

Three-dimensional Helical-rotating Plasma Structures in Beam-generated Partially Magnetized $E \times B$ Plasmas

Jian Chen^{1,*}, Andrew T. Powis², Igor D. Kaganovich², Zhibin Wang^{1,*}

¹*Sino-French Institute of Nuclear Engineering and Technology, Sun Yat-sen University, Zhuhai 519082, P. R. China*

²*Princeton Plasma Physics Laboratory, Princeton NJ 08543, USA*

*Emails: chenjian5@mail.sysu.edu.cn and wangzhibin@mail.sysu.edu.cn

Azimuthal structures emerging in beam-generated partially magnetized $E \times B$ plasmas are investigated using three-dimensional particle-in-cell simulations. Two distinct instability regimes are identified at low pressures. When the gas pressure is sufficiently high, quasi-neutrality is attained and 2D spiral-arm structures form as a result of the development of a lower-hybrid instability, resulting in enhanced cross-field transport. At lower pressures, quasi-neutrality is not achieved and a 3D helical-rotating plasma structure forms due to development of the diocotron instability. Analytical formulas are proposed for the critical threshold pressure between these regimes and for the rotation frequency of the helical structures.

Introduction — Beam-generated partially-magnetized $E \times B$ plasmas with magnetized electrons and unmagnetized ions have emerged as a promising technique for atomic-layer functionalization [1-3]. In such plasmas, macroscopic azimuthally rotating structures with enhanced plasma density are commonly observed [4-12]. These structures form single or multiple spiral arms known as “spokes”. The emergence of these structures results in significantly enhanced particle and energy transport across the magnetic field that can cause unexpected damage to the surfaces being processed. Understanding the formation and dynamics of azimuthal structures is essential for precise control of beam-generated partially-magnetized plasma properties.

Several instabilities have been identified as drivers of azimuthal structure formation. Krall et al. [13] and Hirose et al. [14] theoretically predicted the occurrence of a lower-hybrid instability induced by cross-field current in nonuniform plasmas, which was later confirmed in beam-generated discharge experiments [15]. Another possible driver is the modified Simon-Hoh instability. The Simon-Hoh instability, originally studied by Simon [16] and Hoh [17] for collisional cases, is driven by the relative velocity drift between electrons and ions, arising in systems where the electric field and plasma density gradient satisfy the condition $\mathbf{E} \cdot \nabla n_0 > 0$. However, a modified Simon-Hoh instability exists for collisionless plasmas, where the difference in drift velocity arises due to the large Larmor radius of weakly magnetized ions [18]. Experimental observations of the modified Simon-Hoh instability have been reported in various beam-generated $E \times B$ plasma devices [18-20]. More recently, the centrifugal instability, caused by differences in electron and ion azimuthal velocities

due to inertia, has also been proposed as a formation mechanism for rotating structures in partially magnetized linear plasma machines [21, 22].

In addition to numerous experimental and theoretical efforts, numerical simulations have been indispensable in revealing the formation and dynamics of azimuthal structures during the nonlinear saturation stage [23-30]. While some preliminary 3D simulations have been reported at recent meetings [31, 32], most numerical studies of beam-generated $E \times B$ plasmas have been performed in the 2D transverse dimension, neglecting longitudinal processes (parallel to the magnetic field). This omission overlooks important 3D physics effects, such as the unstable modes with finite parallel wave number and the boundary effects observed in experiments [19, 33], underscoring the need for fully 3D kinetic simulations.

In this letter, we present 3D3V particle-in-cell (PIC) simulations of azimuthal structures in beam-generated partially magnetized $E \times B$ plasmas. Beam electrons are injected into a grounded metal chamber along a uniform longitudinal magnetic field, ionizing neutral helium gas and producing plasma. We identify two regimes, each controlled by different instabilities and their resulting azimuthal structures. These regimes can be distinguished by whether the quasi-neutrality condition is attained. In the quasi-neutral regime, the beam-generated plasma exhibits development of the lower-hybrid instability, forming quasi-2D spiral azimuthal arms. In the non-neutral regime, where ionization is insufficient to sustain quasi-neutrality, the non-neutral plasma is susceptible to a diocotron instability, eventually leading to the collective helical rotation of the entire plasma.

Model— The electron beam-generated plasma in an $E \times B$ device is modeled using the 3D3V LTP-PIC software, an extensively benchmarked [34, 35], explicit electrostatic particle-in-cell (PIC) code. The simulation domain consists of a three-dimensional Cartesian box with transverse dimensions $L_x = L_z = 25$ mm and a longitudinal length $L_y = 200$ mm, with all boundaries grounded and fully absorbing. An electron beam is launched along the $+y$ direction from a small window ($4 \text{ mm} \times 4 \text{ mm}$) at the center of the left boundary with a density of $n_b = 10^{15} \text{ m}^{-3}$, a temperature of $T_b = 5 \text{ eV}$ and an energy of $\mathcal{E}_b = 50 \text{ eV}$. A uniform longitudinal magnetic field of $B = 100 \text{ G}$ is applied and the domain is filled with helium gas at varying pressures. These parameters are motivated by the Princeton Plasma Physics Laboratory (PPPL) experimental setup described in Refs. [33] and [36].

Electron-neutral collisions (elastic scattering, excitation, ionization) and ion-neutral charge exchange collisions are included in the simulations. A cell size $\Delta x = 390 \text{ }\mu\text{m}$ and a time step $\Delta t = 20 \text{ ps}$ are specified to resolve the Debye length ($\lambda_{De} \approx 525 \text{ }\mu\text{m}$), plasma frequency ($\omega_{pe} \approx 1.78 \times 10^9 \text{ s}^{-1}$), and fulfill the Courant–Friedrichs–Lewy condition for beam electrons. The simulation is initialized with a plasma density of $n_0 = 1 \times 10^{15} \text{ m}^{-3}$ and 300 macro-particles per cell for each species. The simulations were run to steady state at

more than 20 μs using 4096 CPU cores on the Perlmutter supercomputer at the National Energy Research Scientific Computing Center (NERSC), typically completing within 2 days.

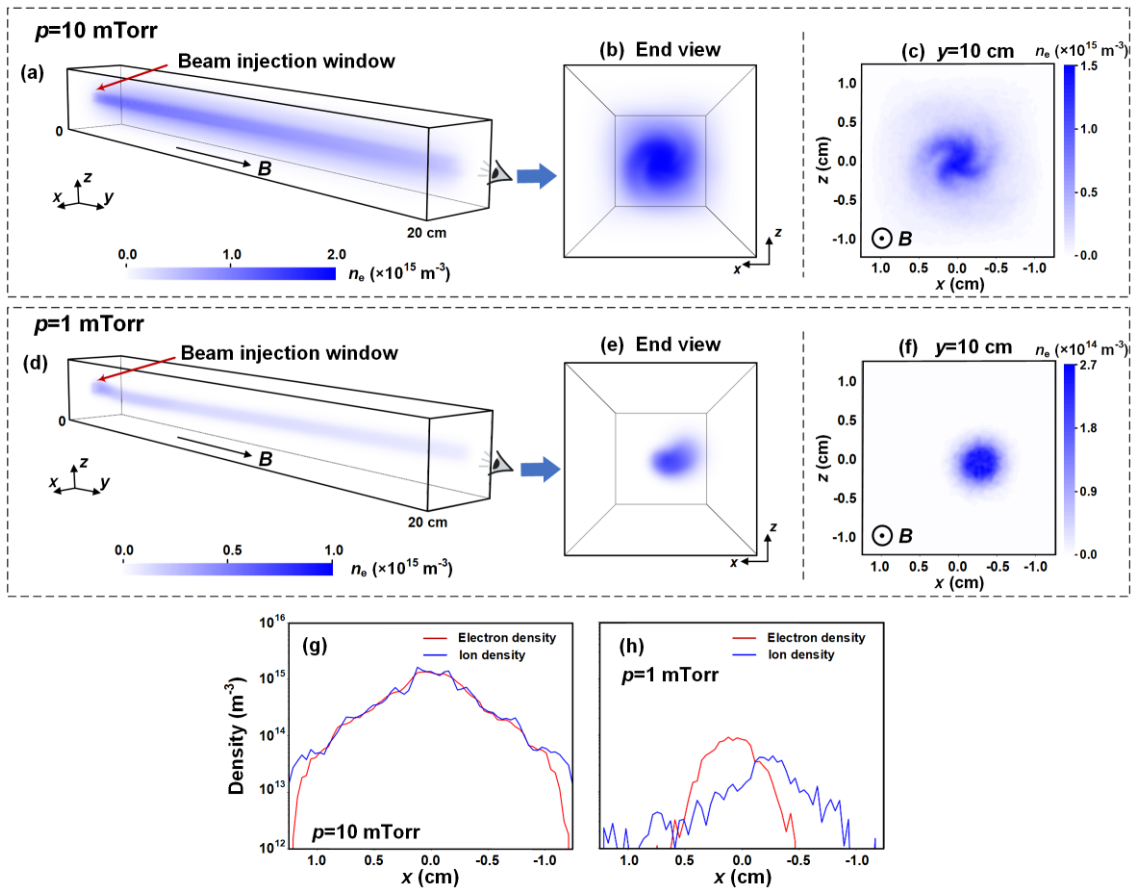


Fig. 1 The first row [subfigures (a) ~ (c)] and the second row [subfigures (d) ~ (f)] show the electron number density at quasi-steady state for the cases with $p=10$ mTorr and $p=1$ mTorr, respectively. Therein, subfigures (a) and (d) show the 3D distribution of electron number density, with the magnitude illustrated in shaded blue. Subfigures (b) and (e) show the end views of (a) and (d) captured by a synthetic diagnostic “camera” near the end of the domain with a 30° view angle. Black lines mark the boundaries (gray lines mark the 30° view angle boundaries). All 3D plots and axial views are generated using the VisIt program [37]. Subfigures (c) and (f) show the color plots of transverse cross sections of electron number density at $y=10$ cm. Subfigures (g) and (h) show the 1D profiles of electron and ion number densities along the line ($y=10$ cm, $z=0$ cm) for the cases with $p=10$ mTorr and $p=1$ mTorr, respectively.

Two regimes with distinct azimuthal structures — By varying the pressure, we identify two regimes characterized by distinct azimuthal structures depicted in Fig. 1. Note that the plots represent the quasi-steady state, where particle production and losses are balanced, and periodic azimuthal rotation persists.

As shown in Fig. 1(a), at $p=10$ mTorr, the rotating plasma primarily concentrates along the axis [the line with the coordinates ($x=0$, $z=0$)]. In contrast, at $p=1$ mTorr, the plasma shifts off-axis, forming a three-dimensional helical-rotating structure [Fig. 1(d)]. This structure has an angular frequency $\omega \approx 5.6$ MHz (see the Fourier spectrum in Section I of the Supplemental material and the plasma dynamics in the Supplemental video [38]). With an eccentric distance of approximately 0.25 cm, this corresponds to a linear velocity of ~ 14

km/s. This off-axis helical structure is suggestive of the electron-hose instability observed with electron beams propagating through ion channels [39], or the transverse two-stream instability [40]. However, unlike the electron-hose and transverse two-stream instabilities, where transverse displacements oscillate in time and space, the instability observed here exhibits rotation as a 3D helical structure with nearly constant eccentricity.

To clarify the different azimuthal dynamics between the two cases, end-view images of the plasma [Figs.1(b) and 1(e)] and transverse profiles of electron density [Figs.1(c) and 1(f)] are provided. In actual experiments, azimuthal dynamics are typically captured by fast cameras at the chamber's end window. We capture these images using a synthetic camera with a 30° cone of vision placed at the end of the domain [Figs.1(b) and 1(e)], corresponding to the integration of electron density along the line of sight. At $p=10$ mTorr, Figs. 1(b) and 1(c) reveal azimuthal structures with curved tails extending from the center, a feature also seen in previous radial-azimuthal simulations [25, 30]. At $p=1$ mTorr, the end-view image [Fig. 1(e)] also reveals spiral structures, resembling the $m=1$ azimuthal “arms” observed in linear plasma machines such as MISTRAL [8-11]. However, comparison with the transverse electron density profile in Fig. 1(f) indicates that these are not genuine 2D azimuthal structures but rather projections of an off-axis 3D helical structure.

These differing plasma behaviors suggest the existence of two distinct regimes. As shown in Figs. 1(g) and 1(h), the most notable distinction lies in whether quasi-neutrality is maintained. At $p=10$ mTorr, electron and ion density profiles are nearly identical (except in the sheath). However, at $p=1$ mTorr, quasi-neutrality breaks, and a displacement between electron and ion columns is clearly evident. This displacement along with electron beam rotation generates a time-dependent electric field that forces ions to collectively rotate lagging behind the electrons. In this Letter, we refer to the above two regimes as the quasi-neutral and non-neutral regimes.

A question naturally arises as to how non-neutrality can be maintained at quasi-steady state in the non-neutral regime. The space charge from the non-neutralized negative electron beam creates a potential well that can trap ionization-produced ions, which could ultimately lead to ion density increasing to the point of quasi-neutrality. However, we show that ions escape from the potential well towards the transverse walls due to the centrifugal effect caused by the collective rotation of both the electron beam and ionization-produced ions, leading to non-neutrality at steady state. More details are provided in Section II of the Supplemental material [38].

Dominant instabilities in the quasi-neutral and non-neutral regimes — The beam-generated plasmas in the quasi-neutral and non-neutral regimes are produced as a result of different instabilities. For illustration, we analyze the first several microseconds of plasma evolution while the instabilities develop and saturate.

In the quasi-neutral regime, as shown in Fig. 2, an $m = 4$ azimuthal mode emerges in the first few microseconds with elongated and curved tails [Fig. 2(a)]. This mode arises from a lower-hybrid instability,

destabilized by a radial density gradient and collisions shortly after beam injection. Given that $k_y \approx 0$, the dispersion relation for the lower-hybrid instability reads [30, 41]

$$k_{\perp}^2 \lambda_{De}^2 = \frac{k_{\perp}^2 c_s^2}{\omega^2} - \frac{\omega^* + k_{\perp}^2 \rho_e^2 (\omega - \omega_E + i\nu_{en})}{\omega - \omega_E + k_{\perp}^2 \rho_e^2 (\omega - \omega_E + i\nu_{en})}, \quad (1)$$

where $\omega^* = -mT_e / (eB_0 r L_n)$, $\omega_E = -mE_r / (rB_0)$, $L_n^{-1} = n'_0 / n_0$ (the prime denotes the derivative in the radial direction), $k_{\perp} \approx k_{\theta} = m/r$ is the perpendicular wave number, $\omega_{ce} = eB_0 / m_e = 1.76 \times 10^9 \text{ s}^{-1}$ is the electron gyrofrequency, n_0 is the equilibrium number density, E_r is the radial electric field strength, $\rho_{ce} = \sqrt{T_e / (m_e \omega_{ce}^2)}$ is the electron Larmor radius, $c_s = \sqrt{T_e / m_i}$ is the ion acoustic speed, and ν_{en} is the electron-neutral collision frequency. In the 2D limit of $k_y \approx 0$, both beam and plasma electrons are assumed to have the same response to the transverse electric field perturbations. Fig. 2(b) presents the Fourier spectrum along with the dispersion relation from Eq. (1). As shown, the Fourier spectrum of the $m=4$ mode matches the theoretical dispersion relation, suggesting that this mode is of the lower-hybrid type generated at the maximum growth rate. As the instability saturates, it stabilizes into the spiral azimuthal structures observed in Figs. 1(b) and 1(c). The local simulation parameters used in these calculations are summarized in Table I.

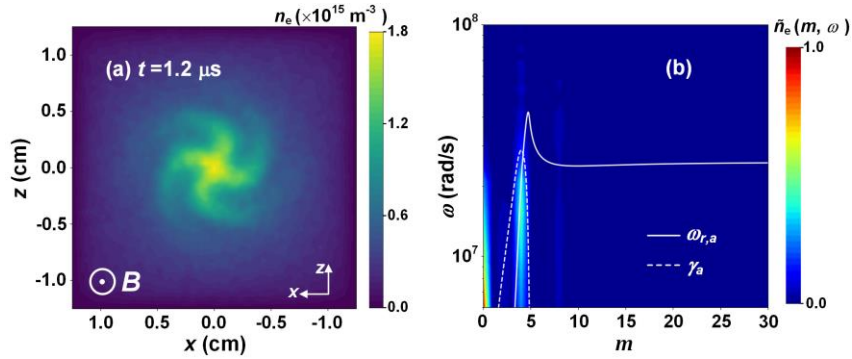


Fig. 2 (a) Electron number density profiles at $y=2 \text{ cm}$ and $t=1.2 \mu\text{s}$, showing the azimuthal mode induced by the lower-hybrid instability. The magnetic field vector is directed outward. (b) Fourier spectrum of azimuthal modes from $0 \mu\text{s}$ to $1.2 \mu\text{s}$. The solid and dashed white lines denote the real frequency, $\omega_{r,a}$, and growth rate, γ_a , versus the azimuthal mode number m , calculated using Eq. (1). The data is taken from the case with $p=10 \text{ mTorr}$.

Table I. Local parameters ($r=0.25 \text{ cm}$, 10 mTorr case) used in the calculation of dispersion relation based on Eq. (1)

Parameters	$n_0 (\text{m}^{-3})$	$T_e (\text{eV})$	$B_0 (\text{Gauss})$	$L_n (\text{cm})$	$E_r (\text{V/m})$	$\nu_{en} (\text{s}^{-1})$
Values	1.5×10^{15}	10	100	-0.25	-1000	1.2×10^7

In contrast, plasma in the non-neutral regime evolves into two intertwined helical columns [Fig. 3(a)], each with a distinct density peak in the transverse profile [Fig. 3(b)]. Electrons near these peaks rotate around them, forming azimuthal vortices [Fig. 3(c)]. These two helical columns not only rotate collectively around

the axis but also interact/compete with each other. Over time, one column fades, while the other grows larger and eventually evolves into the off-axis helical structure observed in Fig. 3(d) and Fig. 1(d). The detailed evolution of this process can be observed in the Supplemental video [38].

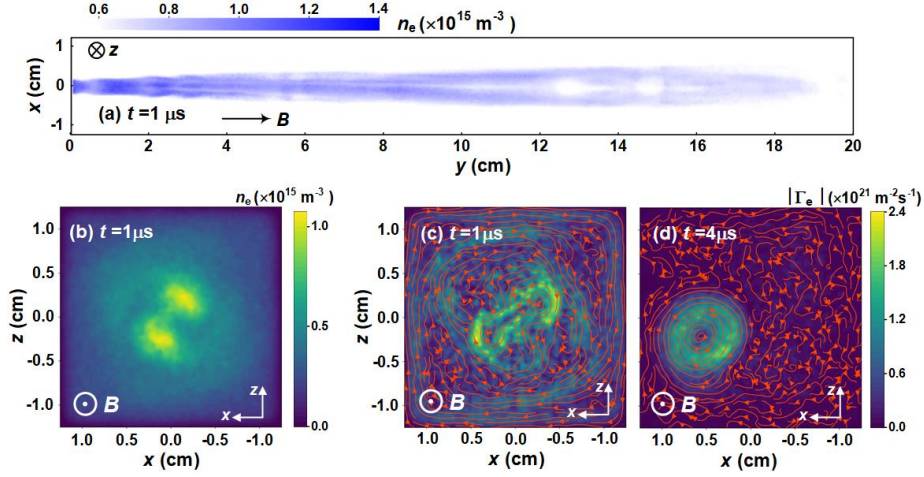


Fig. 3 (a) Transverse view of electron number density stereogram at $t=1 \mu\text{s}$; (b) Profile of electron number density at the slice $y=10 \text{ cm}$ and $t=1 \mu\text{s}$; Streamlines of electron flux at the cross-section $y=10 \text{ cm}$ at $t=1 \mu\text{s}$ (c) and $t=4 \mu\text{s}$ (d).

Generation of the azimuthal vortices is the result of a *diocotron instability*- a Kelvin-Helmholtz-type instability arising from velocity shear generated by space charges [42], i.e., $\nabla \times \vec{v}_E = \frac{e(n_i - n_e)\vec{b}}{\epsilon_0 B}$, which is the key factor leading to the diocotron instability. Similar off-axis diocotron modes have already been observed in a Penning-Malmberg trap [43-48]. Our work presents, to the best of our knowledge, the first 3D simulations showing the whole evolution of a diocotron instability and its relationship to the azimuthal structures.

The stability threshold for the diocotron instability can be calculated by analyzing the eigenvalue equation for the electrostatic potential perturbation, $\delta\phi(r)$, as derived previously in Refs. [42, 49-52]. Neglecting v_{en} , the eigenvalue equation for $\delta\phi(r)$ is given by

$$\begin{aligned} & \frac{1}{r} \frac{\partial}{\partial r} \left[r \left(1 - \frac{\omega_{pe}^2}{\eta_e^2} - \frac{\omega_{pi}^2}{\eta_i^2} \right) \frac{\partial}{\partial r} \delta\phi \right] - \frac{m^2}{r^2} \left(1 - \frac{\omega_{pe}^2}{\eta_e^2} - \frac{\omega_{pi}^2}{\eta_i^2} \right) \delta\phi - k_y^2 \left(1 - \frac{\omega_{pe}^2}{(\omega - k_y v_y - \omega_E)^2} - \frac{\omega_{pi}^2}{\omega^2} \right) \delta\phi \\ & = - \frac{m\delta\phi}{r(\omega - \omega_E)} \frac{\partial}{\partial r} \left[\frac{\omega_{pe}^2}{\eta_e^2} \left(-\omega_{ce} + 2 \frac{v_E}{r} \right) \right] - \frac{m\delta\phi}{r\omega} \frac{\partial}{\partial r} \left[\frac{\omega_{pi}^2}{\eta_i^2} \omega_{ci} \right], \end{aligned} \quad (2)$$

where ω_{pe} and ω_{pi} are the electron and ion plasma frequency, v_y is the axial electron velocity, $v_E = r\omega_E/m = -E_r/B$ is the azimuthal $E \times B$ drift, and

$$\eta_e^2 = (\omega - k_y v_y - \omega_E)^2 - \left(-\omega_{ce} + 2 \frac{v_E}{r} \right) \left[-\omega_{ce} + \frac{1}{r} \frac{\partial}{\partial r} (r v_E) \right], \quad \eta_i^2 = \omega^2 - \omega_{ci}^2. \quad (3)$$

Although the diocotron mode has a finite k_y (i.e., has a helical structure), $k_y \ll k\theta$ and $k_y v_y \ll \omega_E$, and therefore, $k_y v_y$ can be neglected in Eq. (2) and Eq. (3). In addition, considering that within these simulations $\omega_{ci}, \omega_{pi} \ll |\omega -$

$\omega_E \ll \omega_{ce}$, Eq. (3) can be readily reduced to

$$\frac{1}{r} \frac{\partial}{\partial r} \left[r \frac{\partial}{\partial r} \delta\phi \right] - \frac{m^2}{r^2} \delta\phi = - \frac{m\delta\phi}{r(\omega - \omega_E)} \frac{e}{\varepsilon_0 B (1 + \omega_{pe}^2 / \omega_{ce}^2)} \left(\frac{\partial n_{e0}}{\partial r} - \frac{\omega_{pe}^2}{\omega_{ce}^2} \left(\frac{\partial n_{e0}}{\partial r} - \frac{\partial n_{i0}}{\partial r} \right) \right), \quad (4)$$

where $n_{e0}(r)$ is the equilibrium electron density. A similar equation was also obtained in Ref. [52]. As discussed in Refs. [49, 50, 52], for systems without a central conducting wall, instability occurs only if

$$\Lambda = \frac{\partial n_{e0}}{\partial r} - \frac{\omega_{pe}^2}{\omega_{ce}^2} \left(\frac{\partial n_{e0}}{\partial r} - \frac{\partial n_{i0}}{\partial r} \right) \quad (5)$$

changes sign as the radius increases from the center to the boundary. As shown in Section III of the Supplemental material, for the case with $p=1$ mTorr, Λ crosses zero at $r \approx 0.32$ cm, indicating that the diocotron instability can be triggered at this radius (as confirmed by Fig. 3(b)).

Threshold pressure between the quasi-neutral and non-neutral regimes — To estimate the threshold pressure delineating the quasi-neutral and non-neutral regimes, a global model accounting for ion balance is developed. From numerical results one can show that ions produced through electron beam-induced ionization are primarily lost in the radial direction. Given that the observed radial ion density profile in simulations is exponential [see Fig. 1(g)], the ionization balance yields

$$n_b v_{iz} S_{beam} \approx D_{\perp} n_{i0} \exp\left(-\frac{r}{|L_n|}\right) \cdot \frac{2\pi r}{|L_n|}, \quad (6)$$

where v_{iz} represents the electron-impact ionization coefficient which is proportional to the pressure, S_{beam} is the area of beam cross section, n_{i0} is the ion number density at the axis, and D_{\perp} is the perpendicular diffusion coefficient.

To solve Eq. (6), D_{\perp} needs to be determined. As discussed in Section IV of the Supplemental material [38], a large-amplitude fluctuating electric field near the axis significantly enhances radial diffusion. This instability-enhanced D_{\perp} is challenging to estimate analytically because it is sensitive to both the fluctuation levels and large-scale structure formation [53, 54]. To proceed, we consider recent experiments which provide a fitted D_{\perp} using the form of a Bohm diffusion coefficient [36, 55]

$$D_{\perp} \approx \alpha \frac{T_e}{eB}. \quad (7)$$

where α is an anomalous parameter. Experimental observations show that $\alpha \approx 1/60$ near the axis ($r \lesssim |L_n|$) and increases sharply with radius to maintain particle continuity. Although Eq. (7) was obtained at operating pressure different from those in our simulations, D_{\perp} is weakly dependent on pressure when a lower-hybrid instability determines the anomalous diffusion. Therefore, one can substitute Eq. (7) into Eq. (6) and setting $r = |L_n|$, we obtain

$$n_b v_{iz} S_{beam} \approx \frac{\pi}{30} \frac{T_e}{eB} n_{i0} \exp(-1). \quad (8)$$

Solving Eq. (8) yields n_{i0} . To satisfy the quasi-neutrality condition, n_{i0} must exceed the beam density n_b . Consequently, the threshold pressure can be determined by equating n_{i0} to n_b .

In addition to Eq. (7), D_{\perp} may also be estimated via the modified Kadomtsev mixing-length transport coefficient [56-58]

$$D_{\perp} \approx \frac{2.4^2}{2} \left(\frac{\gamma_k}{k_{\perp}^2} \frac{\gamma_k^2}{\omega_k^2 + \gamma_k^2} \right)_{\max}. \quad (9)$$

where γ_k and ω_k are the linear growth rate and real frequency of the Fourier mode k_{\perp} . k_{\perp} is typically chosen to maximize D_{\perp} . Solving Eq. (6) with Eq. (9) provides an alternative estimate of the threshold pressure.

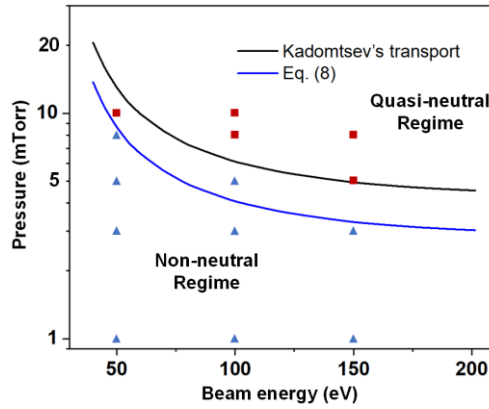


Fig. 4 The value of threshold pressure separating the quasi-neutral and non-neutral regimes as a function of beam energy. The blue line represents the theoretical solution of Eq. (8) with $T_e=10$ eV. The black line represents the theoretical solution obtained by solving Eq. (6) with Eq. (9), using $k_{\perp}=1600$ m^{-1} , $\gamma_k=2.9 \times 10^7$ s^{-1} and $\omega_k=1.6 \times 10^7$ determined from Fig. 2(b), along with the helium ionization cross section data from Ref. [59]. Red square markers indicate simulation cases within the quasi-neutral regime, while blue triangle markers represent simulation cases within the non-neutral regime.

To verify the predictions of threshold pressure, 12 more 3D simulations were conducted across a range of pressures and beam energies, with the results shown in Fig. 4. The blue line represents the solution of Eq. (8), while the black line represents the theoretical solution obtained by solving Eq. (6) with Eq. (9). Kadomtsev's estimate has a nearly 50% difference compared to the experimental fit. The simulation results, denoted by red squares (quasi-neutral regime) and blue triangles (non-neutral regime), show good agreement with both the experimental fit and Kadomtsev's estimate. The deviation for some boundary cases suggests that the precise value of D_{\perp} likely lies between the predictions of Eqs. (7) and (9).

Rotation frequency of the helical structure — In the non-neutral regime, the plasma can be treated as a cloud of net negative charges undergoing collective azimuthal rotation due to the $\mathbf{E}_{eff} \times \mathbf{B}$ drift, where an effective electric field, \mathbf{E}_{eff} , primarily arises from the asymmetric charge distribution. A similar phenomenon

has been reported in previous studies of the diocotron mode in pure electron plasmas [60-62]. Using the image charge method, the angular frequency of the helical structure can be estimated as

$$\omega \approx \frac{|\lambda|}{2\pi\epsilon_0 BR^2}, \quad (10)$$

where $\lambda \approx -\int e(n_e - n_i) dS$ is the linear net charge density, R is half of the transverse length and d is the off-axis distance of the helical structure. The derivation of Eq. (10) can be found in Section V of the Supplemental material [38].

For the case with $p=1$ mTorr, the parameters at $y=10$ cm were found to be $\lambda \approx -6.9 \times 10^{-10}$ C/m and $R=1.25$ cm. Substituting these values into Eq. (10) yields $\omega=8.1$ MHz, which is qualitatively consistent with the simulated value of $\omega=5.6$ MHz. This discrepancy is likely due to the shape of electron density not being ideally cylindrical, thereby introducing additional multipole effects.

Conclusion — In this Letter, we have studied the azimuthal structures forming in partially magnetized beam-generated plasmas using 3D particle-in-cell simulations. Two distinct regimes dominated by different instabilities are identified. In the quasi-neutral regime, the lower-hybrid instability generates spiral arms which define the resulting cross-field transport. In the non-neutral regime, the diocotron instability creates azimuthal vortices, disrupting the beam and resulting in collective helical plasma rotation.

We show that the axial projection of the helical-rotating plasma exhibits behavior similar to that of the spoke, which could lead to misinterpretation of this structure in some experiments, thereby calling for further experimental investigation of 3D effects. We also have proposed and verified the analytical formulas for the critical threshold pressure for transition between the two regimes and for the rotation frequency of the helical plasma, providing guidance for future experiments.

The work of J. Chen and Z. B. Wang was supported by National Natural Science Foundation of China (Grant No. 12305223) and Guangdong Basic and Applied Basic Research Foundation (Grant No. 12305223). The work of A. T. Powis and I. D. Kaganovich at Princeton Plasma Physics Laboratory (PPPL) was supported by US Department of Energy under CRADA agreement between Applied Material Inc. and PPPL. Resources of the National Energy Research Scientific Computing Center (NERSC) were used for high performance computation.

Reference

- [1] F. Zhao, Y. Raitses, X. F. Yang, A. Tan, and C. G. Tully, Carbon **177**, 244 (2021).
- [2] G. M. Petrov, D. R. Boris, E. H. Lock, Tz. B. Petrova, R. F. Fernsler, and S. G. Walton, J. Phys. D: Appl.

- Phys. **48**, 275202 (2015).
- [3] S. G. Walton, D. R. Boris, S. C. Hernández, E. H. Lock, Tz. B. Petrova, G. M. Petrov, and R. F. Fernsler, ECS J. Solid State Sci. Technol. **4**, N5033 (2015).
- [4] J. P. Boeuf, Front. Phys. **2**, 74 (2014).
- [5] M. Panjan, S. Loquai, J. E. Klemberg-Sapieha, and L. Martinu, Plasma Sources Sci. Technol. **24**, 065010 (2015).
- [6] A. Anders, P. Ni and A. Rauch, J. Appl. Phys. **111**, 053304 (2012).
- [7] S. Mazouffre, L. Grimaud, S. Tsikata, K. Matyash, and R. Schneider, Plasma Sources Sci. Technol. **28**, 054002 (2019).
- [8] Th. Pierre, A. Escarguel, D. Guyomarc'h, R. Barni, and C. Riccardi, Phys. Rev. Letts. **92**, 065004 (2004).
- [9] S. Jaeger, T. Pierre, and C. Rebont, Phys. Plasmas **16**, 022304 (2009).
- [10] A. Escarguel, Eur. J. Phys. D **56**, 209 (2010).
- [11] N. Claire, A. Escarguel, C. Rebont, F. Doveil, Phys. Plasmas **25**, 061203 (2018).
- [12] J. -P. Boeuf and B. Chaudhury, Phys. Rev. Letts. **111**, 155005 (2013).
- [13] N. A. Krall and P. C. Liewer, Phys. Rev. A **4**, 2094 (1971).
- [14] A. Hirose and I. Alexeff, Nucl. Fusion **12**, 315 (1972).
- [15] M. Yamada and D. K. Owens, Phys. Rev. Letts. **38**, 1529 (1977).
- [16] A. Simon, Phys. Fluids **6**, 382 (1963).
- [17] F. C. Hoh, Phys. Fluids **6**, 1184 (1963).
- [18] Y. Sakawa, C. Joshi, P. K. Kaw, F. F. Chen, and V. K. Jain, Phys. Fluids B **5**, 1681 (1993).
- [19] E. Rodríguez, V. Skoutnev, Y. Raitses, A. Powis, I. Kaganovich, and A. Smolyakov, Phys. Plasmas **26**, 053503 (2019).
- [20] K. Thomassen, Phys. Fluids **9**, 1836 (1966).
- [21] R. Gueroult, J. -M. Rax, and N. J. Fisch, Phys. Plasmas **24**, 082102 (2017).
- [22] S. Aggarwal, Y. Camenen, A. Escarguel, and A. Poyé, J. Plasmas Phys. **89**, 905890310 (2023).
- [23] A. T. Powis, J. A. Carlsson, I. D. Kaganovich, Y. Raitses, and A. Smolyakov, Phys. Plasmas **25**, 072110 (2018).
- [24] J. Carlsson, I. Kaganovich, A. Powis, Y. Raitses, I. Romadanov, and A. Smolyakov, Phys. Plasmas **25**, 061201 (2018).
- [25] M. Tyushev, M. Papahn Zadeh, V. Sharma, M. Sengupta, Y. Raitses, J.-P. Boeuf, and A. Smolyakov, Phys. Plasmas **30**, 033506 (2023).
- [26] J. -P. Boeuf and M. Takahashi, Phys. Rev. Lett. **124**, 185005 (2020).
- [27] M. Sengupta, A. Smolyakov, and Y. Raitses, J. Appl. Phys. **129**, 223302 (2021).

- [28] R. Kawashima, K. Hara, and K. Komurasaki, *Plasma Sources Sci. Technol.* **27**, 035010 (2018).
- [29] L. Xu, D. Eremin, and R. P. Brinkmann, *Plasma Sources Sci. Technol.* **30**, 075013 (2021).
- [30] R. Lucken, A. Bourdon, M. A. Lieberman, and P. Chabert, *Phys. Plasmas* **26**, 070702 (2019).
- [31] J. Chen, A. T. Powis, and I. Kaganovich, Three-dimensional particle-in-cell simulations of the spoke-like activity in a Penning discharge, *76th Annual Gaseous Electronics Conference (GEC 2023), Ann Arbor, Michigan (2023)*.
- [32] G. Fubiani, L. Garrigues, F. Gaboriau, A. Smolyakov, and Y. Camenen, 3D PIC/MCC modeling of the dynamics of rotating spokes in a Penning discharge, *77th Annual Gaseous Electronics Conference (GEC 2024), San Diego, California (2024)*.
- [33] N. S. Chopra, I. Romadanov, and Y. Raitses, *Plasma Sources Sci. Technol.* **33**, 125003 (2024).
- [34] A. T. Powis and I. D. Kaganovich, *Phys. Plasmas* **31**, 023901 (2024).
- [35] T. Charoy, J. -P. Boeuf, A. Bourdon, J. A. Carlsson, P. Chabert, B. Cuenot, D. Eremin, L. Garrigues, K. Hara, I. D. Kaganovich, et al., *Plasma Sources Sci. Technol.* **28**, 105010 (2019).
- [36] N. S. Chopra, M. P. Zadeh, M. Tyushev, A. Smolyakov, A. Likhanskii, and Y. Raitses, arXiv, 2024. <https://arxiv.org/abs/2412.01675>.
- [37] The latest release and user manuals of VisIt program are available at <https://github.com/visit-dav/visit>.
- [38] See the Supplemental material and Supplemental videos at (link to be added).
- [39] D. H. Whittum, W. M. Sharp, S. S. Yu, M. Lampe, and G. Joyce, *Phys. Rev. Lett.* **67**, 991 (1991).
- [40] R. C. Davidson, I. Kaganovich, H. Qin, E. A. Startsev, D. R. Welch, D. V. Rose, and H. S. Uhm, *Phys. Rev. ST Accel. Beams* **7**, 114801 (2004).
- [41] A. I. Smolyakov, O. Chapurin, W. Frias, O. Koshkarov, I. Romadanov, T. Tang, M. Umansky, Y. Raitses, I. D. Kaganovich, and V. P. Lakhin, *Plasma Phys. Control. Fusion* **59**, 014041 (2017).
- [42] R. C. Davidson, *Physics of Nonneutral Plasmas*, Chap. 6, pp. 242 (Addison-Wesley, Reading, MA, 1990).
- [43] W. D. White, J. H. Malmberg, and C. F. Driscoll, *Phys. Rev. Letts.* **49**, 1822 (1982).
- [44] C. F. Driscoll, *Phys. Rev. Letts.* **64**, 645 (1990).
- [45] J. M. Finn, D. del-Castillo-Negrete, D. C. Barnes, *Phys. Rev. Letts.* **84**, 2401 (2000).
- [46] J. Fajans, E. Gilson, and L. Friedland, *Phys. Rev. Letts.* **82**, 4444 (1999).
- [47] C. F. Driscoll and K. S. Fine, *Phys. Fluids B* **2**, 1359 (1990).
- [48] G. Bettega, B. Parolo, R. Pozzoli, and M. Romé, *J. Appl. Phys.* **105**, 053303 (2009).
- [49] R. H. Levy, *Phys. Fluids* **8**, 1288 (1965).
- [50] R. J. Briggs, J. D. Daugherty, and R. H. Levy, *Phys. Fluids* **13**, 421 (1970).
- [51] S. A. Prasad and J. H. Malmberg, *Phys. Fluids* **29**, 2196 (1986).
- [52] A. A. Litvak and N. J. Fisch, *Phys. Plasmas* **11**, 1379 (2004).

- [53] T. Lafleur, S. D. Baalrud, and P. Chabert, *Phys. Plasmas* **23**, 053503 (2016).
- [54] M. Krämer, N. Sollich, and J. Dietrich, *J. Plasma Phys.* **39**, 447 (1988).
- [55] N. S. Chopra, Boundary-induced kinetic effects in low temperature E×B plasmas, Ph.D. thesis, Princeton University, 2024.
- [56] B. B. Kadomtsev, *Plasma Turbulence*, Chap. 4, pp. 107 (Academic Press, London, 1965).
- [57] J. W. Connor and O. P. Pogutse, *Plasma Phys. Control. Fusion* **43**, 155 (2001).
- [58] J. Weiland, *Plasma Phys. Rep.* **42**, 502 (2015).
- [59] M. M. Turner, A. Derzsi, Z. Donkó, D. Eremin, S. J. Kelly, T. Lafleur, and T. Mussenbrock, *Phys. Plasmas* **20**, 013507 (2013).
- [60] K. S. Fine, *Phys. Fluids B* **4**, 3981 (1992).
- [61] K. S. Fine, C. F. Driscoll, and J. H. Malmberg, *Phys. Rev. Letts.* **63**, 2232 (1989).
- [62] K. S. Fine and C. F. Driscoll, *Phys. Plasmas* **5**, 601 (1998).

Supplemental material of “Three-dimensional helical-rotating plasma structures in beam-generated partially magnetized $E \times B$ plasmas”

Jian Chen^{1,*}, Andrew T. Powis², Igor D. Kaganovich², Zhibin Wang^{1,*}

¹*Sino-French Institute of Nuclear Engineering and Technology, Sun Yat-sen University, Zhuhai 519082, P. R. China*

²*Princeton Plasma Physics Laboratory, Princeton NJ 08543, USA*

*Emails: chenjian5@mail.sysu.edu.cn and wangzhh8@mail.sysu.edu.cn

Contents

I. Fourier spectrum of the helical plasma structure	1
II. Transverse ion loss due to centrifugal forces	2
III. Profile of Λ triggering the diocotron instability	3
IV. Instability-enhanced diffusion in the quasi-neutral regime	4
V. Estimating the rotation frequency of the helical structure using the image method	6
VI. Description of Supplemental videos	8

I. Fourier spectrum of the helical plasma structure

Figs. S1(a)~(c) depict the “camera” view of the helical-rotating plasma structure at different times, showing the projected electron density. The dynamics resemble an $m=1$ azimuthal spoke, which could potentially lead to a misinterpretation of this structure in some experiments. Figure S1(d) displays the Fourier spectrum of the

electron density fluctuations caused by the rotation of the helical plasma structure, exhibiting a pronounced frequency around $\omega \approx 5.6$ MHz.

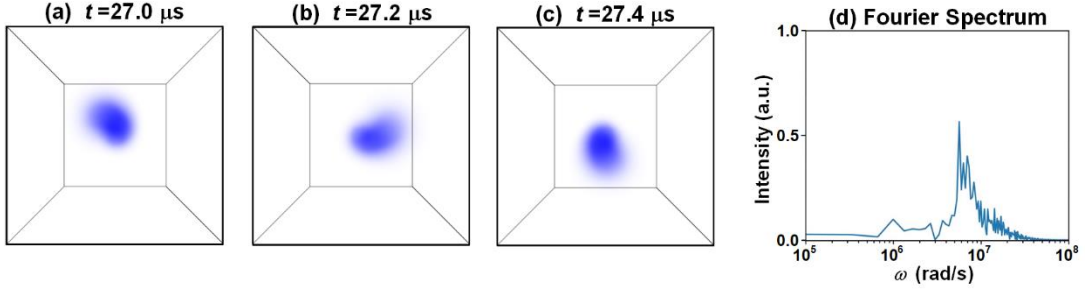


Fig. S1 Subfigures (a), (b) and (c) depict the end views of the helical-rotating plasma structure at $t=27.0 \mu\text{s}$, $t=27.2 \mu\text{s}$ and $t=27.4 \mu\text{s}$, respectively. The end views are captured by a synthetic diagnostic “camera” located near the end of the domain with a 30° view angle. Black lines mark the boundaries (gray lines mark the 30° view angle boundaries). Subfigure (d) presents the Fourier spectrum of electron density fluctuation caused by the rotation of the helical plasma structure. The electron density data used in the Fourier transformation were recorded by a probe at the point (0.4 cm, 2.0 cm, 0 cm). All the data were recorded from the case with $p=1$ mTorr.

II. Transverse ion loss due to centrifugal forces in the non-neutral regime

In an electron beam-plasma discharge, the negative charge of the electron beam creates a potential well which confines ions produced by ionization. This leads to an increasing ion density over time and ultimately the formation of a quasi-neutral plasma. However, we observed that at lower pressure an ambipolar quasi-neutral plasma does not form and offer an explanation for this observation here. Figs. S2(a)~S2(c) show that not only electrons but also ions collectively rotate off the beam axis. This rotation is induced as ions experience kicks caused by the rotating potential well generated by the net negative charge of the electron beam. Therefore, the ion flux is driven by two competing effects: the action of the inward electric field produced by the negative space charge of the electron beam and by an outward directed centrifugal force.

As the helical plasma rotates off-axis azimuthally, newly-produced ions experience an outward centrifugal force that eject them from the potential well. The effective potential including the centrifugal potential reads

$$\phi^* = \phi + \phi_{\text{centrifugal}} = \phi - \frac{m_i \omega^2 r^2}{2e}, \quad (\text{S1})$$

where $\omega \approx 5.6$ MHz denotes the angular frequency of the helical plasma structure. The effective potential profile is shown in Figs. S2(d)~S2(f), where the solid circles indicate the high ion density regions, corresponding to the density profiles in Figs. S2(a)~S2(c). The effective potential, ϕ^* , decreases outwards - as indicated by the arrow - confirming that ions can escape toward the walls. Note that the gradient of ϕ^* also has an azimuthal component, providing evidence that the kick of ions by the rotating potential well contributes to ion rotation.

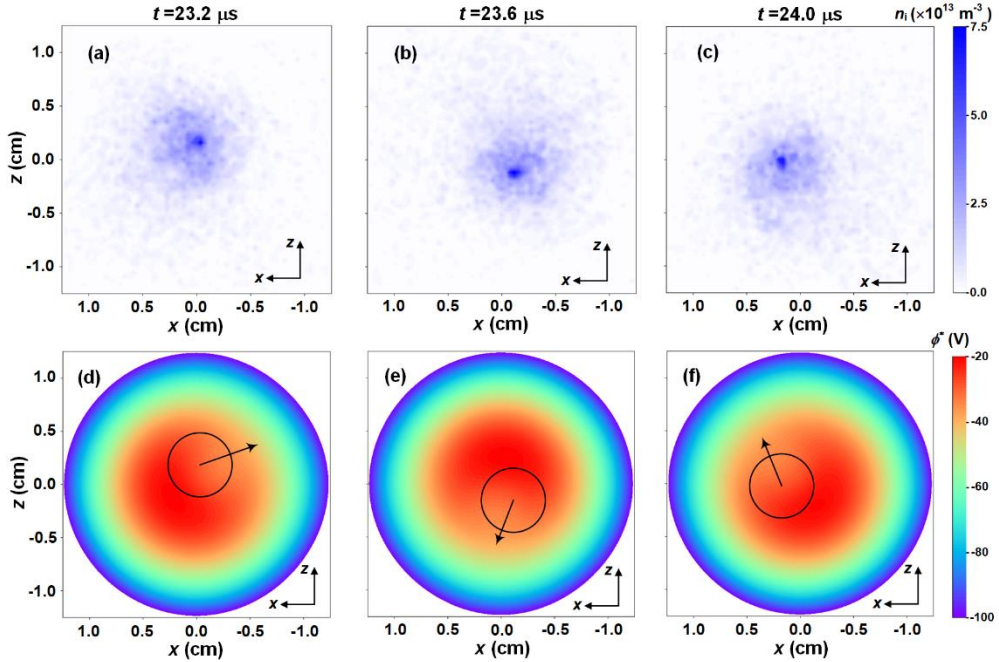


Fig. S2 Profiles of ion number density and effective potential profile $\phi^* = \phi - m_i \omega^2 r^2 / 2e$ at $y=10$ cm at different snapshots for the case with $p=1$ mTorr (non-neutral regime). The solid circles, delineates the high ion density regions shown in (a)-(c), and the arrow indicates the direction of decreasing ϕ^* .

III. Profile of Λ triggering the diocotron instability

Fig. S3 shows the radial profile of Λ (see Eq. (5) in the main text) at $y=0.02$ cm for the case with $p=1$ mTorr. The profile of Λ was calculated using the averaged electron and ion density profiles over the first 200 nanoseconds of the simulation. The transverse plane $y=0.02$ cm was selected because it marks the location where the diocotron

instability initiates and begins to split the beam. As one can see, Λ crosses zero at approximately $r \approx 0.32$ cm, indicating that the diocotron instability can be triggered at this radius due to resonance (as confirmed by Fig. 3(b) in the main text).

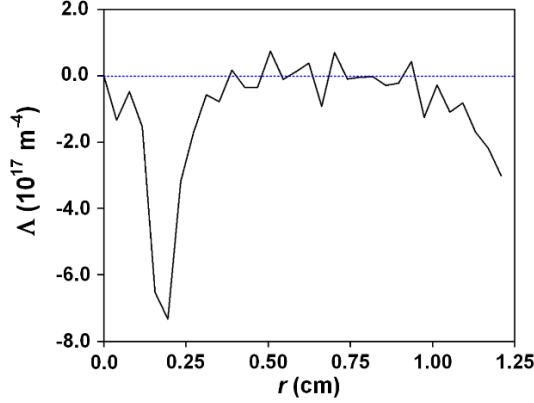


Fig. S3 Radial profile of Λ at $y=0.02$ cm for the case with $p=1$ mTorr. The profile of Λ was calculated using the averaged electron and ion density profiles over the first 200 nanoseconds.

IV. Instability-enhanced diffusion in the quasi-neutral regime

As explained in the main text, the quasi-neutral and non-neutral regimes are primarily distinguished by the quasi-neutrality condition (whether it is attained or not). Therefore, the value of the threshold pressure delineating the two regimes can be regarded as the minimum pressure at which quasi-neutrality is maintained, and can be analyzed via transport calculations in the quasi-neutral regime.

Fig. S4 shows the electron and ion number density profiles, as well as the electrostatic potential at quasi-steady state for the case with $p=10$ mTorr, corresponding to the quasi-neutral regime. In this regime, the density exhibits an exponentially decreasing profile. Within the central region ($r < 0.75$ cm), the mean electric field remains relatively weak, whereas a strong fluctuating electric field is observed, resulting in instability-enhanced radial diffusion of particles. While at the periphery ($r > 0.75$ cm), a mean electric field emerges, accelerating ions.

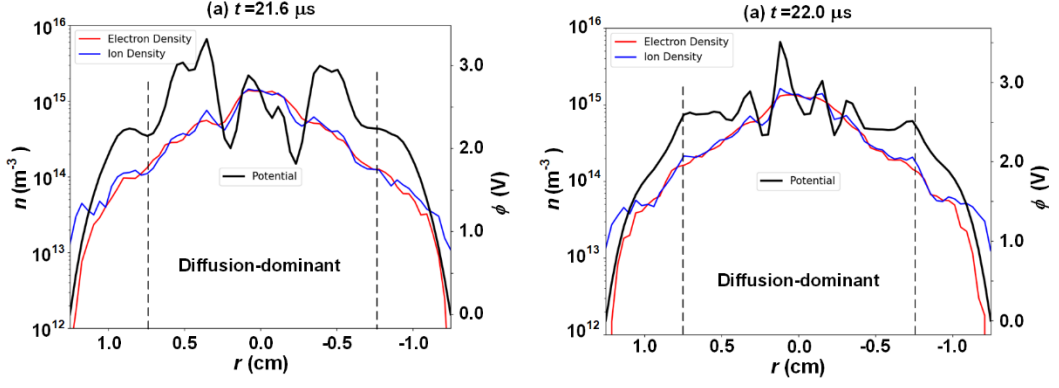


Fig. S4 Profiles of electron and ion number densities and electrostatic potential for the quasi-steady state case with $p=10$ mTorr. In the central region ($r < 0.75$ cm, approximately $3|L_n|$), a strong fluctuating electric field is observed and the radial ion transport is dominated by the instability-enhanced diffusion. At the periphery, a mean electric field emerges, accelerating ions and leading to mobility-dominated transport.

At quasi-steady state, the ion balance gives

$$n_b v_{iz} S_{beam} = \Gamma_{ir} \cdot S, \quad (\text{S2})$$

where v_{iz} represents the electron-impact ionization coefficient, S_{beam} is the area of the beam cross section, Γ_{ir} is the outward radial ion flux and $S=2\pi r$ is the enclosed surface area. Here, it is assumed that ions are predominantly generated via beam electron-impact ionization and lost through radial transport. Such assumptions neglect the ionization caused by the beam-produced plasma electrons and ion loss through the front and end walls, which is acceptable for the large aspect ratio of our system.

Considering the radial transport shown in Fig. S4, the ion balance equation can be simplified by focusing on the enclosed surface within the diffusion-dominated region and assuming an exponentially decreasing density profile. This yields Eq. (6) in the main text

$$n_b v_{iz} S_{beam} = D_{\perp} n_{i0} \exp\left(-\frac{r}{|L_n|}\right) \cdot \frac{2\pi r}{|L_n|}, \quad (\text{S3})$$

where $L_n = n_0 / n'_0$ is the gradient length and D_{\perp} is the perpendicular diffusion coefficient. It should be noted that D_{\perp} varies with radius to ensure continuity, which has been confirmed in recent experiments [1, 2].

V. Estimating the rotation frequency of the helical structure using the image method

The first step in estimating the rotation frequency of the helical structure is to determine the effective electric field E_{eff} acting on the plasma. This effective electric field arises primarily from the asymmetric charge distribution caused by the off-axis rotation of the plasma, which can be estimated using the image method.

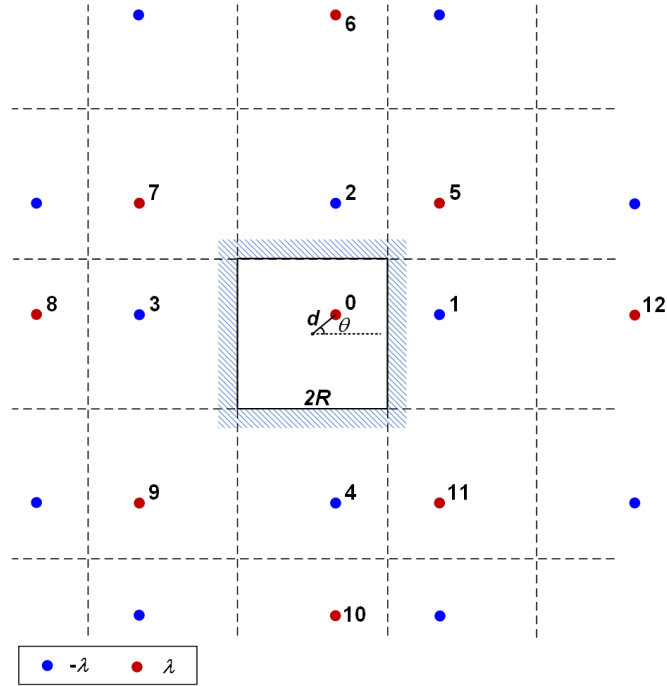


Fig. S5 Charge images for a real line charge in a square box. The red and blue dots denote the line charges with λ and $-\lambda$, respectively.

For the cases considered in this study, where the pitch of the helical plasma is much larger than the eccentricity d , the system can be modeled as a long line charge (Charge 0) with linear charge density $\lambda \approx -\int e(n_e - n_i) dS$ confined within a square box, as shown in Fig. S5. This configuration leads to an infinite number of image charges, created by reflecting both the real and image charges and flipping their signs with each reflection. The red and blue dots denote the line charges with λ and $-\lambda$, respectively.

Let the real charge (Charge 0) have the coordinate $\mathbf{r}_0 = d \cos \theta \mathbf{e}_x + d \sin \theta \mathbf{e}_y$. Then, the coordinates of the images with λ and $-\lambda$ are given by

$$\begin{cases} \mathbf{r}_{-\lambda} = \begin{cases} (4mR + 2R - d \cos \theta) \mathbf{e}_x + (4nR + d \sin \theta) \mathbf{e}_y \\ (4mR + d \cos \theta) \mathbf{e}_x + (4nR + 2R - d \sin \theta) \mathbf{e}_y \end{cases} \\ \mathbf{r}_\lambda = \begin{cases} (4mR + d \cos \theta) \mathbf{e}_x + (4nR + d \sin \theta) \mathbf{e}_y \\ (4mR + 2R - d \cos \theta) \mathbf{e}_x + (4nR + 2R - d \sin \theta) \mathbf{e}_y \end{cases} \end{cases}, m, n \in \mathbb{Z} \text{ and } (m, n) \neq (0, 0), \quad (\text{S4})$$

where R is half of the side length of the square box, m and n are arbitrary integers. m and n cannot both be zero, as this would correspond to the position of the real charge itself. The effective electric field \mathbf{E}_{eff} is then the superposition of the fields generated by all the image charges on the real charge (Charge 0)

$$\mathbf{E}_{\text{eff}} = \sum_{m, n \in \mathbb{Z}, (m, n) \neq (0, 0)}^{\infty} \left(\frac{\lambda (\mathbf{r}_\lambda - \mathbf{r}_0)}{2\pi\epsilon_0 |\mathbf{r}_\lambda - \mathbf{r}_0|^2} - \frac{\lambda (\mathbf{r}_{-\lambda} - \mathbf{r}_0)}{2\pi\epsilon_0 |\mathbf{r}_{-\lambda} - \mathbf{r}_0|^2} \right). \quad (\text{S5})$$

This expression is computationally complex, as it requires summing the contributions from an infinite number of images. However, the calculation can be simplified by considering only the contributions from the nearest images, specifically those formed by one- and two-time reflections (i.e. Charges 1~12 in Fig. S5). These nearest images are the most significant because the electric field decays with distance.

It is readily proved that the electric field generated by the four one-time-reflection images (Charges 1~4) is

$$\mathbf{E}_{1\sim 4} = -\frac{\lambda}{2\pi\epsilon_0} \frac{d \cos \theta}{(R^2 - d^2 \cos^2 \theta)} \mathbf{e}_x - \frac{\lambda}{2\pi\epsilon_0} \frac{d \sin \theta}{(R^2 - d^2 \sin^2 \theta)} \mathbf{e}_y. \quad (\text{S6})$$

The electric field due to the eight two-time-reflection images (Charges 5~12) is

$$\mathbf{E}_{5\sim 12} = \frac{\lambda}{2\pi\epsilon_0} \frac{d^3 \sin \theta \sin 2\theta}{(R^4 - d^4 \sin^2 2\theta)} \mathbf{e}_x + \frac{\lambda}{2\pi\epsilon_0} \frac{d \cos \theta \sin 2\theta}{(R^4 - d^4 \sin^2 2\theta)} \mathbf{e}_y. \quad (\text{S7})$$

For the cases investigated in this work, R is typically several times larger than d . Therefore, the contribution from the images in the second reflection group (Charges 5~12) is negligible (on the order of d^2/R^2 relative to $\mathbf{E}_{1\sim 4}$), allowing us to approximate the effective electric field as:

$$\mathbf{E}_{\text{eff}} \approx -\frac{\lambda}{2\pi\epsilon_0} \frac{d \cos \theta}{R^2} \mathbf{e}_x - \frac{\lambda}{2\pi\epsilon_0} \frac{d \sin \theta}{R^2} \mathbf{e}_y, \quad (\text{S8})$$

where the d^2 term in the denominator has been omitted. Eq. (S8) shows that \mathbf{E}_{eff} points

in the radial direction and generates the $\mathbf{E}_{\text{eff}} \times \mathbf{B}$ drift, which supports azimuthal rotation of the plasma. Consequently, the angular frequency of the helical plasma can be estimated as

$$\omega \approx \frac{|\lambda|}{2\pi\epsilon_0 BR^2}. \quad (\text{S9})$$

Note that Eq. (S9) gives the same estimate as that derived for a cylindrical chamber [3].

VI. Description of Supplemental videos

Supplemental videos I and II titled “10mTorr_3D” and “1mTorr_3D” show the 3D views of electron number density for the cases with $p=10$ mTorr and $p=1$ mTorr.

Supplemental videos III and IV titled “10mTorr_end” and “1mTorr_end” show the end views of electron number density for the cases with $p=10$ mTorr and $p=1$ mTorr.

Reference

- [1] N. S. Chopra, M. P. Zadeh, M. Tyushev, A. Smolyakov, A. Likhanskii, and Y. Raitses, arXiv, 2024. <https://arxiv.org/abs/2412.01675>.
- [2] N. S. Chopra, Boundary-induced kinetic effects in low temperature $\mathbf{E} \times \mathbf{B}$ plasmas, Ph.D. thesis, Princeton University, 2024.
- [3] K. S. Fine, Phys. Fluids B **4**, 3981 (1992).